Influence of modelling hypotheses on strength assessment of CFRP stepped repairs

Jean-Baptiste Orsatelli, Eric Paroissien, Frédéric Lachaud, Sébastien Schwartz

Influence of modelling hypotheses on strength assessment of CFRP stepped repairs

Jean-Baptiste Orsatelli[1,2*], Eric Paroissien[1], Frédéric Lachaud[1], Sébastien Schwartz[1]

[1] *Institut Clément Ader (ICA), Université de Toulouse, ISAE-SUPAERO, INSA, IMT MINES ALBI, UTIII, CNRS, 3 Rue Caroline Aigle, 31400 Toulouse, France*

[2] *DGA Techniques Aéronautiques, 47 rue Saint-Jean, 31130 Balma, France*

*To whom correspondence should be addressed: Tel. (+33)562575012, E-mail: jean-baptiste.orsatelli@isae-supaero.fr

Abstract – Composite stepped repairs can achieve high strength recovery without the addition of bolts or fasteners to the structure. They are therefore a major issue in the field of aerospace composite structure damage repair. However, there is no standardized method to design this type of repairs. Many analytical, semi-analytical and finite element models were proposed throughout the years to predict the strength of stepped repairs, using various hypotheses and simplifications. The aim of this paper is to investigate the influence of modelling hypotheses on stress distribution and strength prediction of composite stepped repairs. Five simplified stepped joint models using macro-element (ME) modelling and finite element method (FE) are compared to a full 3D FE model of a stepped repaired panel. The influence of step length and adhesive fracture toughness was investigated to determine the field of validity of each model. Among FE models, it was shown that modelling the equivalent joint under 2D generalized plain strain gives a very close strength prediction to the 3D stepped repair model while saving computation time. Simplified macro-element models under bar or beam hypotheses are fairly close to the results of FE modelling, but the deviation between those and FE is sensitive to step length and adhesive fracture toughness.

Keywords*: composite material, FEM, macro-element, cohesive zone modelling, adhesive bonding, scarf repair*

1 Introduction

Composite materials have seen their use increased largely in aeronautical structures during the last decades. Nonetheless, those materials may experience damage during their service life that need to be addressed in order to restore the initial strength of the structure. One could cite impacts as a frequent source of damage to aeronautical composite parts. They can for example occur due to tool drop, ground collision, lightning strike or bird strike. As it is not economically sustainable always to replace the damaged parts, the ability to repair composite structures is a major concern. Additionally, since carbon fibre composite materials are difficult to recycle, the ecological impact of replacing an entire part is significant, making repairs also important for ecological reasons. Bonded flush repairs are a very efficient type of repair for composite structures, as they provide increased joint strength compared to doubler repairs, while keeping a smooth aerodynamic surface [1]. The two most common types of flush repairs are scarf repairs (i.e. adherends smoothly machined in a scarf shape) and stepped repairs (i.e. adherends machined in a stepped shape). They allow keeping a smooth external surface and do not require drilling and adding bolts, and subsequently adding mass and stress concentrations, to the original structure. However, there is no current standardized method to design a bonded joint, and the problem is even more complicated when it comes to scarf or stepped repairs because of the varying stiffness of the adherends along the bondline due to plies drop off. This is why, during the recent years, various modelling approaches were explored to design flush repairs. Because of the complexity of a full three-dimensional (3D) model of a flush repair, most of the literature is focused on the analysis of the equivalent joint, which is a 2D representation of the highest loaded section of the 3D repair (Figure 1). In the first place, analytical and semi-analytical models coupled to simple criteria such as maximum or average stress were proposed [2]. Strain based criteria were then introduced to give better account for the non-linear behaviour of the adhesive material [3]. With the development of finite element (FE) and the

increase of available computing power, high fidelity 3D models are now more common [4]. Thanks to cohesive zone modelling (CZM) and continuum damage mechanics, it has become possible to compute the response of a flush repair until failure based on the fracture energy of the adhesive material and composite laminates. Among the papers that achieved strength prediction of flush repairs, many modelling approaches were proposed with various levels of geometrical simplification and types of elements. The main ones are: (i)1 layer of shell elements for the whole laminate [5], (ii) 1 shell element per ply [6] and (iii) 4 brick elements per ply [7, 8]. The use of explicit solvers [8] is popular in flush repairs FE models because of convergence issues of implicit solvers when reaching brutal failure of the repair. Most studies achieve less than 10% deviation between predicted strength and experimental testing [9]. However, each study sticks to a given set of hypotheses when modelling flush repairs, making it difficult to assess the influence of modelling hypotheses on the predicted response of the structure.

Although 3D FE modelling and CZM allow performing high-fidelity simulations, there is a need for less computation-intensive tools to design flush repairs. Following this trend, new studies on semi-analytical modelling of stepped joints [10] were released. Beyond all simplified models of flush repairs lies the question of knowing if the equivalent flush joint can be representative for the load-carrying capacity of a 3D repair. This question is a matter of discussion in the literature [11, 12], but latest papers are going towards the idea that the equivalent joint approach is valid. For instance, there is an agreement on the fact that the stress state in a flush joint is very close to the one in the highest loaded section of a flush repair [13]. A recent comparative study [14] on different levels of modelling of scarf repairs confirmed that the stress concentration factor in the most loaded section of a 3D scarf repair is close to the one in 2D scarf joints models. To the author's knowledge, no studies have performed a comparison between strength predictions made by different flush repair modelling strategies. Hence, this paper attempts to fill this gap. It focuses on stepped repairs rather than scarf repairs, because an

industrial wet-layup repair is generally likely to be closer to a stepped configuration than a scarf configuration due to plies drop-off [15]. This paper investigates the influence of modelling hypotheses on the predicted behaviour of a stepped repair in terms of bondline stress and failure strength. Different models are compared, going from 1D stepped joint to full 3D stepped repair model, in order the determine to what extent a simplified stepped joint (Figure 1b) model can be representative for the behaviour of a stepped repaired panel (Figure 1a).

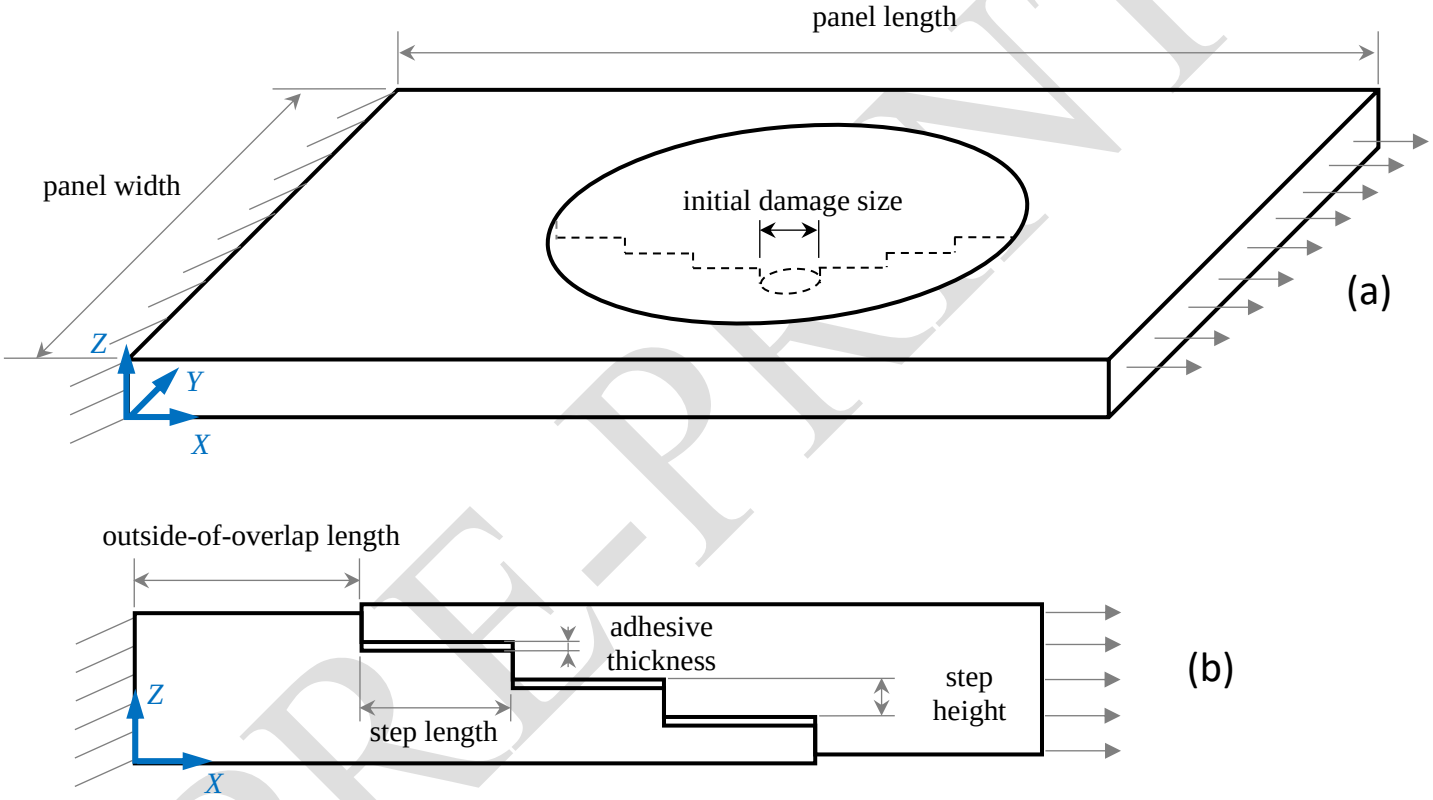

Figure 1: Schematic representation of a stepped repair loaded in tension with parameters, loading and axis system. (a) Stepped repair panel. (b) Equivalent stepped joint.

2 Methodology

2.1 Problem definition

The idea is to propose a comparative study of six different semi-analytical and numerical models using macro-element (ME) modelling and Finite Element (FE) modelling:

(i) ME 1D bar stepped joint (SJ1D bar);

(ii) ME 1D beam stepped joint (SJ1D beam);

(iii) FE plane strain stepped joint (SJ2D PS);

(iv) FE generalized plane strain stepped joint (SJ2D GPS);

(v) FE 3D stepped joint (SJ3D-shell);

(vi) FE 3D stepped repair panel (SR3D-shell).

The first five of them are different modelling approaches of the equivalent stepped joint to the most loaded section of the SR3D-shell model (Figure 1). Uniaxial tension loading is chosen for this study. A range of step length and adhesive fracture toughness is tested for each model to explore the field of validity of each model. Geometrical and material parameters need to be common to all models and hence are described first in this section, whereas implementation of semi-analytical and numerical models is described next.

Geometrical parameters of the stepped repair and its equivalent stepped joint are given in Table 1. The repair is chosen to be centred on the panel for the 3D configuration. Step length varies in a range of 3 mm to 12 mm and each step is one-ply-deep. From an experimental point of view, machining one-ply-deep steps through the whole thickness of a composite laminate is challenging. A novel machining technique has been developed to perform in-situ stepped repairs. It uses water-jet abrasion instead of traditional hand abrasion, making the machining process faster and more reliable [16, 17]. In terms of equivalent scarf angle based on the ratio between total repair thickness and length, tested configurations go from 5.2° to 1.3° angles. This range is near the 3° angle used as a rule of thumb to design flush repairs. G939/M18, a carbon/epoxy woven laminate, is chosen as the reference material for both parent laminates and repair patch, with the same layup of $[45, 0, 45, 0]_s$ for both two. The thickness of each ply is 0.24 mm, which therefore leads to a total thickness of the laminates of 1.92 mm. A matching layup is chosen for the repair, meaning that each ply of the repair patch matches the orientation of the ply of the parent structure it is placed against (Figure 2). In-plane elastic properties of

G939/M18 are given in Table 2. Out-of-plane Young modulus E_{33} and Poisson ratios ν_{13} and ν_{23} are not needed because the analysis that are performed in the following sections rely on bar, beam, or shell (plane stress) models. They come from experimental testing of this material by DGA Aeronautical Systems and are in good agreement with available manufacturer data [18]. Adhesive material properties are given in Table 3. They are not the properties of any particular adhesive material because the idea is to explore a range of adhesive fracture toughness. Therefore, stiffness values, failure stresses and layer thickness are fixed at typical values of an epoxy adhesive with heated curing process. A range of G_{IIC} from 0.25 kJ/m² to 8 kJ/m² is chosen to be explored, while keeping a constant ratio $G_{\mathrm{IC}} = G_{\mathrm{IIC}}/2$. A triangular traction-separation law shape is chosen for the behaviour of the adhesive (Figure 3) in terms of interface stress as function of displacement jump, with linear mixed-mode behaviour. Displacement jump $\delta_{i,e}$ ($\delta_{i,f}$) at initiation (propagation) are deduced from the other parameters to obtain a triangular law shape. As trapezoidal laws are more often used to model the behaviour of ductile adhesives,

a discussion on the influence of the law shapes on the results of this study is provided in section 3.3.1.

Table 1: Stepped repair geometrical parameters.

Parameter (defined in Figure 1)	Value
Panel length	450 mm
Panel width	300 mm
Initial damage diameter	30 mm
Outside of overlap length	50 mm
Number of steps	7
Step height	0.24 mm
Step length	{3,4,6,8,10,12} mm

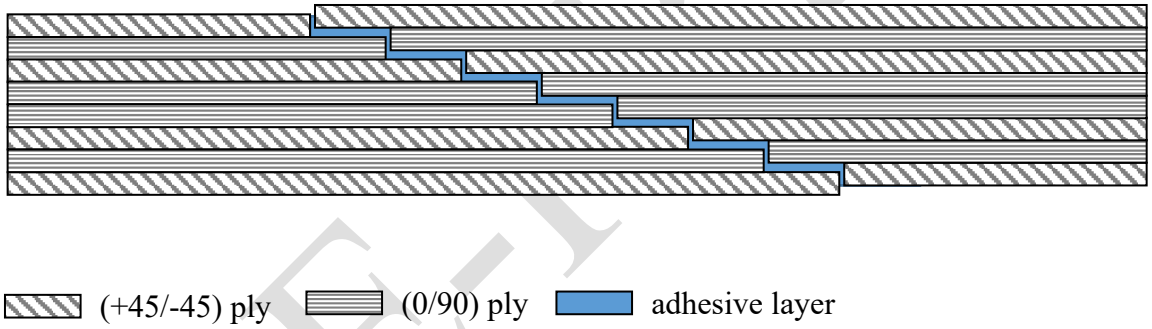

Figure 2: Stepped joint with matching layup

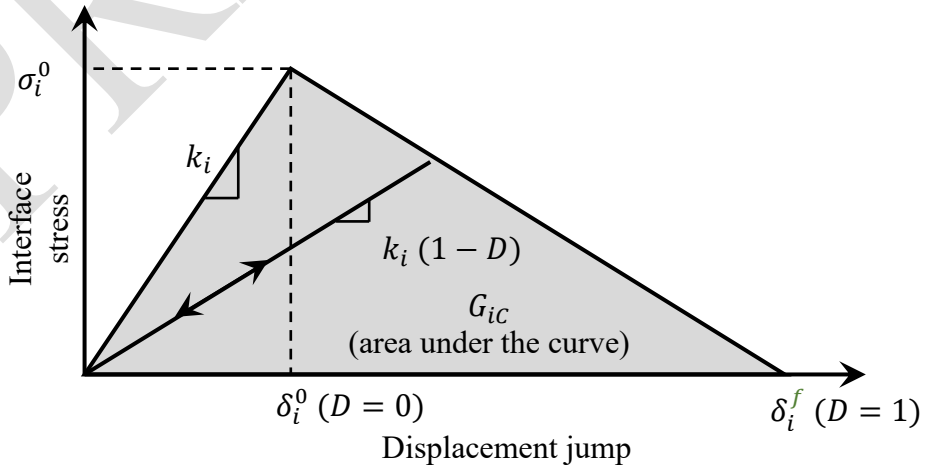

Figure 3 : Cohesive behavior model with triangular traction separation law

Table 2 : Mechanical properties for composite lamina G939/M18

Property	Symbol (units)	Value
Young modulus	$E_{11} = E_{22}$ (MPa)	60000
Poisson ratio	ν_{12}	0.05
Shear modulus	G_{12} (MPa)	4200
	$G_{13} = G_{23}$ (MPa)	4000

Table 3: Mechanical properties for adhesive material

Property	Symbol (units)	Value
Young Modulus	E (MPa)	2400
Shear modulus	G (MPa)	800
Mode II fracture toughness	G_{IIC} (kJ/m^2)	{0.25, 0.5, 1, 2, 4}
Mode I fracture toughness	G_{IC}(kJ/m^2)	G_{IIC} /2
Interface tensile strength	σ_{I}^0 (MPa)	48
Interface shear strength	σ_{II}^0 (MPa)	40
Adhesive layer thickness	t_a (mm)	0.12

No fracture parameters are provided for the composite material because composite failure is not modelled in this study. To design a stepped repair, one could begin by ensuring that the load-carrying capacity of the bonded-joint is higher that the strength of the material needing to be repaired, without considering the coupling between composite fracture and adhesive layer failure. Hence, this paper focuses on the strength prediction of the bonded joint as a simplified design approach and does not address composite failure.

2.2 Macro-element modelling

2.2.1 ME presentation

ME is a semi-analytical method that allows solving configurations of bonded joints with no closed-form solution available because of certain geometrical or material configurations. Especially, it handles non-linear behaviour of the adhesive, such as triangular traction-separation law. It was therefore chosen as a 1D semi-analytical approach to be compared to FE modelling, as it is less computational-heavy than the latter and allows using CZM-like behaviour of the adhesive layer. A ME is a 4-node brick element, but it differs from a standard FE by integrating constitutive and local equilibrium equations of the adherends and the adhesive. It models the behaviour of a single overlap between two adherends. Two different types of ME are used in this study: 1D-bar elements with 1 degree of freedom at each node and 1D-beam elements with 3 degrees of freedom at each node (Figure 4). In the 1D-bar ME, the nodal displacement vector is:

$$U_e = \begin{pmatrix} u_1(0) \\ u_2(0) \\ u_1(\Delta) \\ u_2(\Delta) \end{pmatrix} \quad (1)$$

where u_i is the displacement of the neutral line of the adherend i. The nodal force vector is:

$$F_e = \begin{pmatrix} -N_1(0) \\ -N_2(0) \\ N_1(\Delta) \\ N_2(\Delta) \end{pmatrix} \quad (2)$$

where N_i is the tension / compression internal force in adherend i. The formulation of a 1D-bar ME is detailed hereafter for the comfort of the reader: it is the simplest possible to obtain because each node has only one degree of freedom. The formulation of a 1D-beam ME can be obtained following the same principle [19], but requires more work because of the three degrees of freedom at each node. For the purpose of this section, the axis system *(x,y)* is defined in (Figure 4) and different from the one defined in (Figure 1).

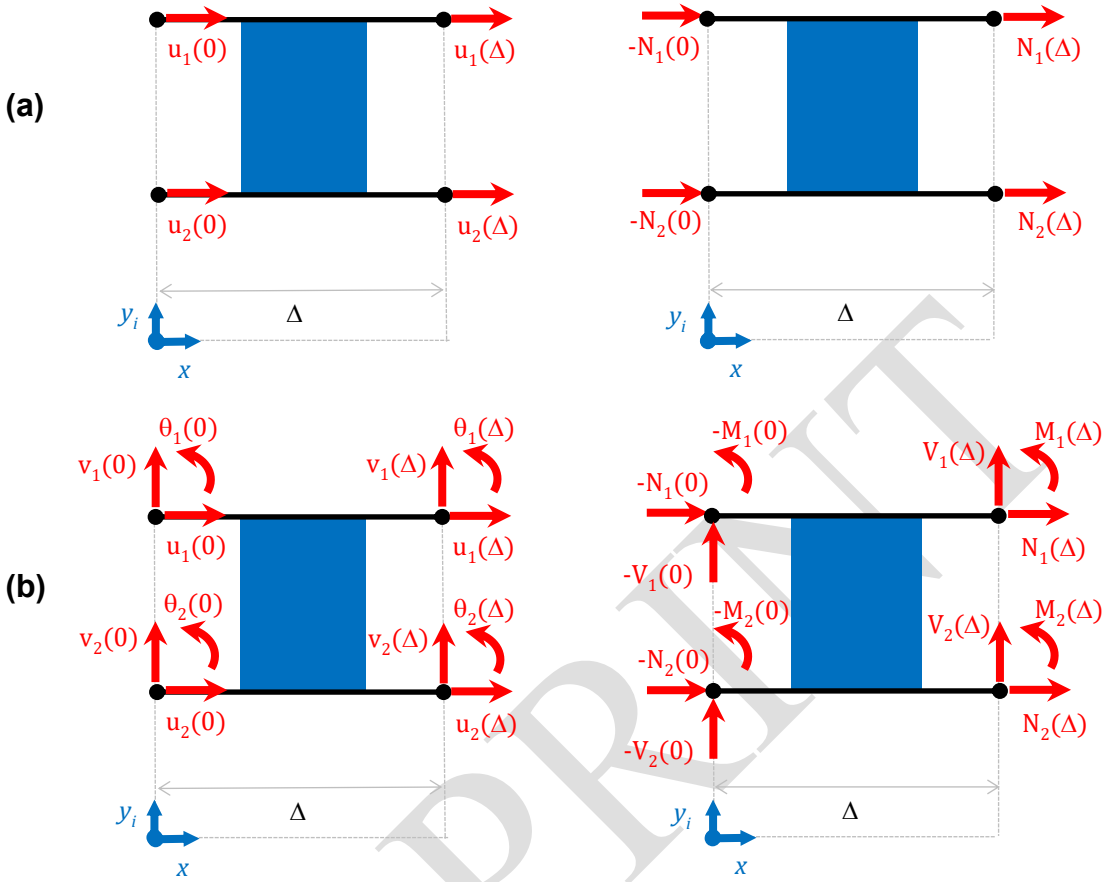

Figure 4: Macro-elements degree of freedom and nodal forces. (a) bonded-bar ME. (b) bonded-beam ME.

2.2.2 Elementary stiffness matrix of 1D bar ME

A 1D-bar ME is obtained by writing the local equilibrium of a single lap-joint (Figure 5) under quasi-static loading and small displacements hypotheses. The adherends are supposed to be made of homogeneous linear elastic material and are modelled as bars. The adhesive layer is modelled as a shear spring foundation. These hypotheses cause the shear stress in the adhesive layer to be constant through the thickness, and the adherends to be loaded in pure tension.

The local equilibrium of each adherends is:

$$\frac{dN_i}{dx} = (-1)^i bT \quad i = 1,2 \tag{3}$$

where b is the width of the joint and T the shear stress in the adhesive layer. Modelling adherends as bars implies that transverse shear deformation of the adherends is neglected. Moreover, adherends are homogeneous. Their constitutive equations are then:

$$N_i = A_i \frac{du_i}{dx} \Leftrightarrow \frac{du_i}{dx} = \frac{N_i}{A_i} \quad i = 1,2 \tag{4}$$

where $A_i = be_iE_i$ is the membrane stiffness, e_i the thickness and E_i the Young's modulus of the adherend i.

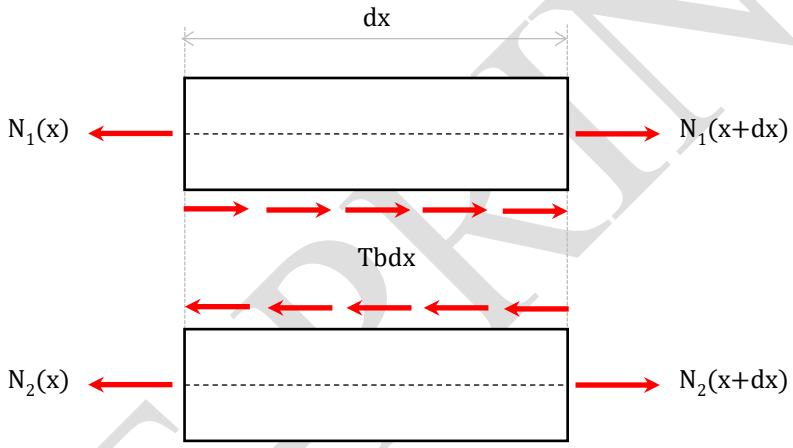

Figure 5: Local equilibrium of a single lap joint

Under small displacements hypothesis, the constitutive relationship of the adhesive layer is written:

$$T = G\frac{u_2 - u_1}{t_a} = \frac{G}{t_a}\Delta_u \tag{5}$$

where Δ_u is the relative longitudinal displacement of the adherends, t_a the adhesive layer thickness and G the adhesive shear modulus.

By writing the derivative of (1) and combining it with (2) and (3), the differential system is obtained:

$$\begin{cases} \dfrac{d^2u_1}{dx^2} = -\dfrac{1}{e_1E_1}\dfrac{G}{t_a}\Delta_u \\ \dfrac{d^2u_2}{dx^2} = -\dfrac{1}{e_2E_2}\dfrac{G}{t_a}\Delta_u \end{cases} \Leftrightarrow \begin{cases} \dfrac{d^2\Delta_u}{dx^2} = \dfrac{G}{t_a}\left(\dfrac{1}{e_1E_1}+\dfrac{1}{e_2E_2}\right)\Delta_u = \eta^2\Delta_u \\ \dfrac{d^2(u_1+u_2)}{dx^2} = -\dfrac{G}{t_a}\left(\dfrac{1}{e_1E_1}+\dfrac{1}{e_2E_2}\right)\Delta_u = -\chi\eta^2\Delta_u = -\chi\dfrac{d^2\Delta_u}{dx^2} \end{cases} \quad (6)$$

where:

$$\eta^2 = \frac{G}{t_a}\left(\frac{1}{e_1E_1}+\frac{1}{e_2E_2}\right) \quad (7)$$

$$\xi = \frac{e_2E_2}{e_1E_1} \quad (8)$$

$$\chi = \frac{\xi-1}{\xi+1} \quad (9)$$

η governs the solution of the equations and χ and ξ are adimensional terms relative to the unbalance between the adherends stiffnesses. Solving the differential system brings the displacements:

$$\begin{pmatrix} u_1 \\ u_2 \end{pmatrix} = \frac{1}{2}\begin{pmatrix} 1 & x & -(1+\chi)e^{-\eta x} & -(1+\chi)e^{\eta x} \\ 1 & x & (1-\chi)e^{-\eta x} & (1-\chi)e^{\eta x} \end{pmatrix} C \quad (10)$$

$$C = \begin{pmatrix} c_1 \\ c_2 \\ c_3 \\ c_4 \end{pmatrix} \quad (11)$$

where the c_i are four integration constants. The aim is then to determine the stiffness matrix K_e that links the displacement vector U_e to the nodal force vector F_e such that $F_e = K_eU_e$. Using the constitutive relationships in equations (3) and (4), two coupling matrices L_e and D_e^{-1} are obtained by writing $C = D_e^{-1}U_e$ and $F_e = L_eC$ (Appendix A). The elementary stiffness matrix is then written:

$$K_e = L_eD_e^{-1} = \frac{1}{1+\xi}\frac{A_2}{\Delta}\begin{pmatrix} \dfrac{\eta\Delta}{\tanh\eta\Delta}+\dfrac{1}{\xi} & 1-\dfrac{\eta\Delta}{\tanh\eta\Delta} & -\dfrac{\eta\Delta}{\sinh\eta\Delta}-\dfrac{1}{\xi} & \dfrac{\eta\Delta}{\sinh\eta\Delta}-1 \\ 1-\dfrac{\eta\Delta}{\tanh\eta\Delta} & \dfrac{\eta\Delta}{\tanh\eta\Delta}+\xi & \dfrac{\eta\Delta}{\sinh\eta\Delta}-1 & -\dfrac{\eta\Delta}{\sinh\eta\Delta}-\xi \\ -\dfrac{\eta\Delta}{\sinh\eta\Delta}-\dfrac{1}{\xi} & \dfrac{\eta\Delta}{\sinh\eta\Delta}-1 & \dfrac{\eta\Delta}{\tanh\eta\Delta}+\dfrac{1}{\xi} & 1-\dfrac{\eta\Delta}{\tanh\eta\Delta} \\ \dfrac{\eta\Delta}{\sinh\eta\Delta}-1 & -\dfrac{\eta\Delta}{\sinh\eta\Delta}-\xi & 1-\dfrac{\eta\Delta}{\tanh\eta\Delta} & \dfrac{\eta\Delta}{\tanh\eta\Delta}+\xi \end{pmatrix} \quad (12)$$

where Δ is the length of the bonded-bar ME (Figure 4).

2.2.3 Stepped joint modelling

This paper introduces a novel approach to model a stepped joint using the ME modelling. A stepped joint can be seen as succession of single-lap joints with adherends of different stiffnesses and the same adhesive layer. Hence, this new modelling approach involved using a series of bonded ME for each step (Figure 6). Bonded-bar ME were used in the SJ1D bar model, and bonded-beam ME in the SJ1D beam model. The portions of the stepped joint that are outside of the overlap area were modelled by bar or beam elements respectively.

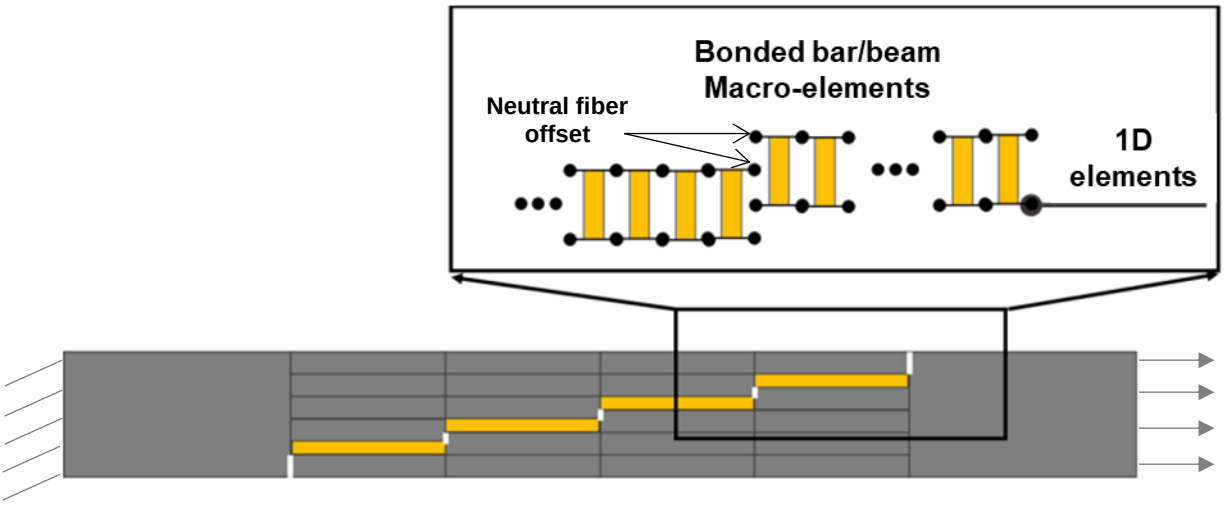

Figure 6 : Macro-element modelling of a stepped joint and boundary conditions

As shown is section 2.2.2, 1D-bar MEs only allow longitudinal displacement of the adherends. Hence, the SJ1D model is a numerical implementation of a classical shear-lag model, with CZM behaviour of the adhesive layer. 1D-beam MEs use an Euler-Bernoulli beam behaviour with membrane-flexion coupling to deal with the laminate nature of the adherends [19]. Because each step has a different number of plies on each side of the adhesive layer, the membrane and flexion stiffness of each one had to be computed individually. However, this involves a discontinuity in material properties and a neutral fibre offset when going from one step to

another. Kinematic constraints had to be added to link each step to the next one to deal with it. (Figure 7).

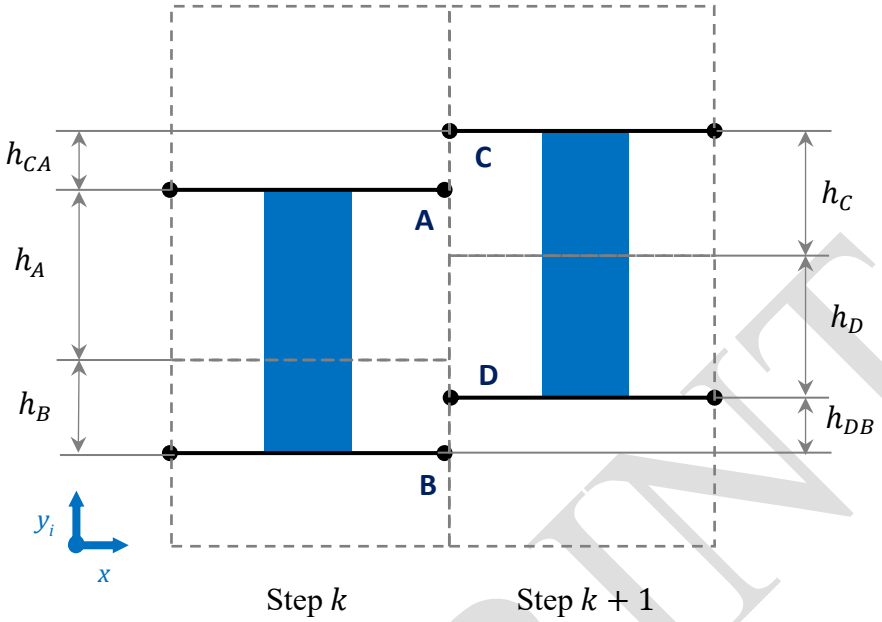

Figure 7: Neutral fibre offset between two steps

A reduction matrix R was written to remove one of both nodes attached together in the structural stiffness matrix, which becomes $K_r = RK_eR^t$. When using 1D-bar MEs, there was no need to consider the neutral fibre offset between each step because there is not out of plane degrees of freedom. Therefore, each step was attached to the next one by writing:

$$\begin{cases} u_A = u_C \\ u_B = u_D \end{cases} \tag{13}$$

The reduction matrix was then written:

$$\begin{pmatrix} u_A \\ u_B \end{pmatrix} = R \begin{pmatrix} u_A \\ u_B \\ u_C \\ u_D \end{pmatrix} \Leftrightarrow R = \begin{pmatrix} 0 & 0 & 1 & 0 \\ 0 & 0 & 0 & 1 \end{pmatrix} \tag{14}$$

When using 1D-beam MEs, the neutral fibre offset had to be taken in account when attaching the ME together. Rotations were supposed to be equal at the junctions of two steps:

$$\begin{cases} \theta_A = \theta_C \\ \theta_B = \theta_D \end{cases} \tag{15}$$

which is a reasonable assumption under Euler-Bernoulli kinematics. Out of plane displacements were supposed to be equal as well:

$$\begin{cases} v_A = v_C \\ v_B = v_D \end{cases} \tag{16}$$

It leads to say that the peel stress is continuous at the junction of two steps due to the peeling stiffness of the adhesive being constant. The kinematic constraints binding axial displacement were written to keep a continuous shear stress T_k at the junction of two steps k and $k+1$:

$$T_{k+1} = T_k \Leftrightarrow (u_B - u_A - h_A\theta_A - h_B\theta_B) = (u_D - u_C - h_D\theta_D - h_C\theta_C) \tag{17}$$

Then, using the neutral line offset h_{CA} (Figure 7) the kinematic conditions were obtained:

$$\begin{cases} u_A = u_C - h_{CA}\theta_C \\ u_B = u_D - h_{BD}\theta_D \end{cases} \tag{18}$$

The reduction matrix was then written:

$$\begin{pmatrix} u_A \\ u_B \\ v_A \\ v_B \\ \theta_A \\ \theta_B \end{pmatrix} = R \begin{pmatrix} u_A \\ u_B \\ u_C \\ u_D \\ v_A \\ v_B \\ v_C \\ v_D \\ \theta_A \\ \theta_B \\ \theta_C \\ \theta_D \end{pmatrix} \Leftrightarrow R = \begin{pmatrix} 0 & 0 & 1 & 0 & 0 & 0 & 0 & 0 & 0 & 0 & -h_{CA} & 0 \\ 0 & 0 & 0 & 1 & 0 & 0 & 0 & 0 & 0 & 0 & 0 & -h_{BD} \\ 0 & 0 & 0 & 0 & 0 & 0 & 1 & 0 & 0 & 0 & 0 & 0 \\ 0 & 0 & 0 & 0 & 0 & 0 & 0 & 1 & 0 & 0 & 0 & 0 \\ 0 & 0 & 0 & 0 & 0 & 0 & 0 & 0 & 0 & 0 & 1 & 0 \\ 0 & 0 & 0 & 0 & 0 & 0 & 0 & 0 & 0 & 0 & 0 & 1 \end{pmatrix} \tag{19}$$

Each step can be linked to the next one using the reduction matrix R, and the whole stepped-joint was obtained this way. Loading was then progressively applied in form of an imposed displacement at one end (Figure 6).

2.2.4 Non-linear computation management

Adherends properties were computed for each step based on classical laminated theory with properties defined in Table 2. Adhesive layer properties given in Table 3 were used in SJ1D bar and SJ1D beam models with a triangular traction-separation law shape (Figure 3), initial

interface stiffnesses $k_{\mathrm{I}} = E/t_a$ and $k_{\mathrm{II}} = G/t_a$, and linear mixed-mode behaviour. The use of cohesive law is a particular case of nonlinear behaviour, because a nonlinear computation is required to predict the current damage state. The nonlinear algorithm used is detailed in [20]. Nevertheless, a very brief overview is provided hereafter to explain the principle of the resolution.

The algorithm is based on the Newton-Raphson method. It uses the secant stiffness matrix with an update at each iteration. The imposed displacements are applied linearly as function of the numerical time by increments of 0.05 mm. The secant matrix update consists in updating the adhesive interface stiffnesses k_{I} and k_{II} according to the value of the damage parameter D.

The triangular mixed-mode law used a quadratic stress initiation criterion:

$$\left(\frac{\langle\sigma_n\rangle}{\sigma_{\mathrm{I}}^0}\right)^2 + \left(\frac{\langle\sigma_s\rangle}{\sigma_{\mathrm{II}}^0}\right)^2 = 1 \tag{20}$$

where σ_n (σ_s) is interface normal (shear) stress. The evolution law is based on linear interaction between each mode:

$$\frac{G_{\mathrm{I}}}{G_{\mathrm{IC}}} + \frac{G_{\mathrm{II}}}{G_{\mathrm{IIC}}} = 1 \tag{21}$$

All the details on mixed-mode propagation law can be found in [20]. The classical assumption that its projections on pure mode are triangular was made. Because each ME has one damage parameter associated with each pair of nodes, the highest of both values is assigned to the ME to compute its material law at the next iteration. Finally, the secant matrix is updated using interface stiffness $(1 - D)k_i$ instead of k_i, where $i \in \{\mathrm{I}, \mathrm{II}\}$.

2.3 Finite element analysis

2.3.1 Geometry and properties

Four FE models developed with ABAQUS/Standard were used to test different levels of numerical modelling: SJ2D plane strain, SJ2D GPS, SJ3D-shell and SR3D-shell. The implicit

solver with full Newton Raphson scheme was chosen as it is able to handle CZM nonlinear behaviour and while being faster than the explicit solver for such models. SJ2D PS, SJ2D GPS and SJ3D-shell models use the stepped joint geometry (Figure 1 b), whereas SR3D-shell used the stepped repair configuration (Figure 1 a). Axis system (X,Y,Z) and boundary conditions are also defined in Figure 1. The X-axis was aligned the direction of the load, the Y-axis was oriented through the width of the models and the Z-axis through the thickness of the laminates. Geometrical parameter values are given in Table 1.

The same element types and properties were used in the four models. Each composite ply was modelled by one layer of continuum shell elements, which are eight-nodes-elements using a shell formulation and therefore plane stress state, with reduced integration scheme. Linear elastic behaviour with properties described in Table 2 were used for the adherends of the stepped joint, and for the parent plate and repair patch of the stepped repair. Adhesive layers were modelled by one layer of brick cohesive elements. Kinematic constraints were used to enforce the continuity of displacement between the adherends and the adhesive layers. Mixed-mode traction separation behaviour was used in the cohesive elements of the adhesive layers, with properties given in Table 3. A triangular law shape was used (Figure 2) with stiffnesses $k_{\mathrm{I}} = E/t_a$ in mode I and $k_{\mathrm{II}} = G/t_a$. The mixed mode law was defined using quadratic stress initiation criterion (eq. 20) and linear energetic evolution law (eq. 21), to ensure that the FE models use the same cohesive laws as the ME models. The influence of the propagation criterion used is discussed is subsection 3.3.1.

2.3.2 Mesh and boundary conditions

Three different meshes were created **(**Figure 8):

The first mesh was for both the SJ2D PS and SJ2D GPS models. It was created in 3D space with of only one layer of elements in the width, and an arbitrary width value of 1 mm was used.

To create a plane strain state, a boundary condition imposing a transverse displacement UY = 0 was applied on both side faces of the 2D plane strain model. 2D elements were not used because ABAQUS does not allow the input of 45° plies properties whose in-plane global axis Poisson's ratio is 0.75. The stepped joint was fully clamped on one end, while applying the load in form of an imposed displacement UX on the other end until disbonding. The SJ2D GPS model was identical to the 2D plane strain mode in every way, expect that a transverse displacement UY = 0 was imposed one only of the side faces while a constant transverse displacement UY was enforced on the whole other side face. It was achieved by constraining all the nodes on the second face to follow to UY displacement of the first node of the first step in the one of the adherends. It should be noted that the choice of the reference node does not matter here, thus it could have been any other node on the constrained face.

The SJ3D-shell model was identical to the SJ2D models except it had a width of 20 mm to be representative for a test coupon and 20 elements through the width. The side edges remained free, and load was applied identically: one edge clamped, and one loaded with an imposed displacement UX.

The SR3D-shell model was the only one to include the parent plate and the circular patch in the middle. Thanks to the symmetries of the problem, preserved by the stacking sequence only containing (0/90°) and (+45°/-45°) woven plies, only a quarter of the complete stepped repaired panel was modelled. A number of 30 elements were used along the quadrant. A zero displacement condition was imposed orthogonally to the plans of symmetry. The load was also applied in form of an imposed displacement UX until patch disbonding.

A coarse element length of 1 mm was used outside the bonded area, in order to save computation time. A finer element size, determined thanks to a mesh study, needed to be used in the bonded joint area.

2D Stepped joint in plane strain or GPS (1 element in the width)

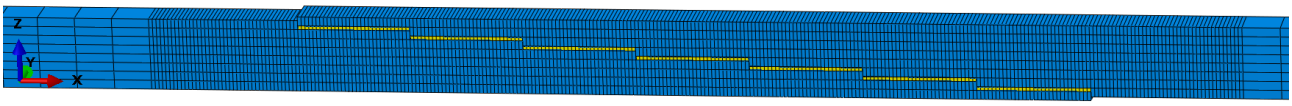

3D Stepped joint (full width)

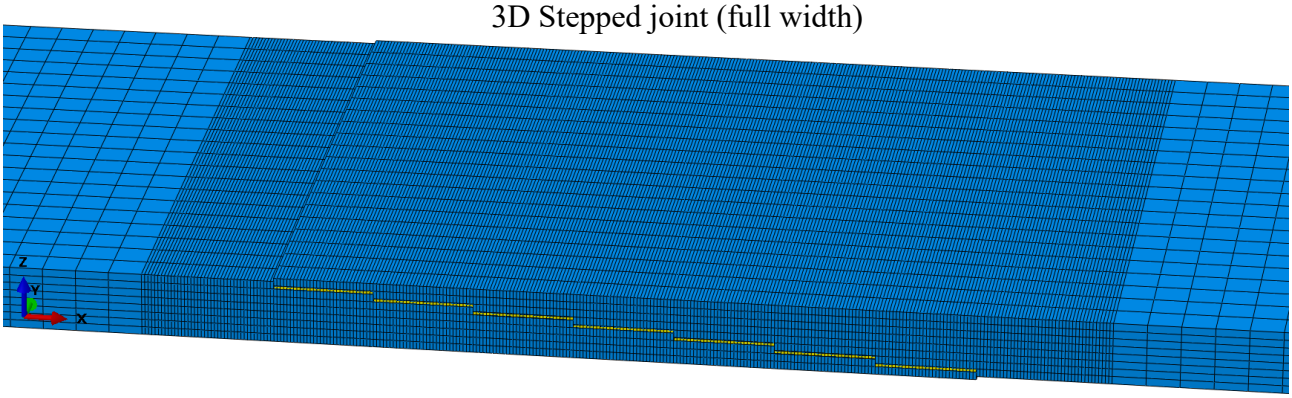

3D Stepped repair (quarter plate)

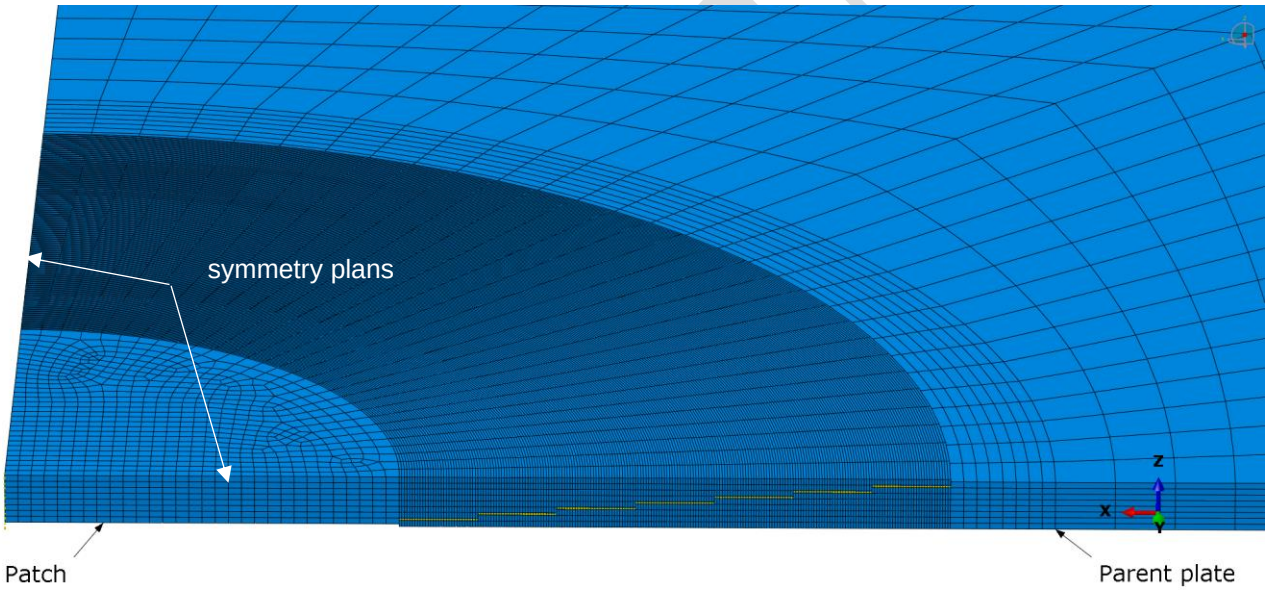

Figure 8 : Meshes used in FE models.

2.4 Convergence study

A mesh study was carried out on each of the six models presented in this study. Because the process zone length in the adhesive layer decreases when the adhesive fracture energy decreases, a more brittle adhesive material requires a finer mesh if adhesive stiffness and maximum interface stress remain unchanged. Hence, this mesh study was performed with the smallest energy in the parameters range $G_{\mathrm{IIC}} = 0.25\ \mathrm{kJ/m^2}$, and with the shortest step length

considered, which is 3 mm. Bonded joint strength was chosen as the convergence criterion for the mesh study.

Under an element length of 0.2 mm, there was very little effect of mesh density on joint strength in FE models (Figure 9). The same was true for ME models under an element length of 0.1 mm. Finally, element size of 0.1 mm was retained for both ME and FE models. Even though 0.2 mm could have been sufficient for FE models, a minimum of three elements in the length of the process zone is needed to ensure good modelling of crack propagation in the adhesive layer [21]. Having enough elements in the process zone allows to compute a stable growth of the process zone and propagation of debonding. Because typical process zone observed was about 0.3mm long, the choice of an element size 0.1 mm seemed more appropriate.

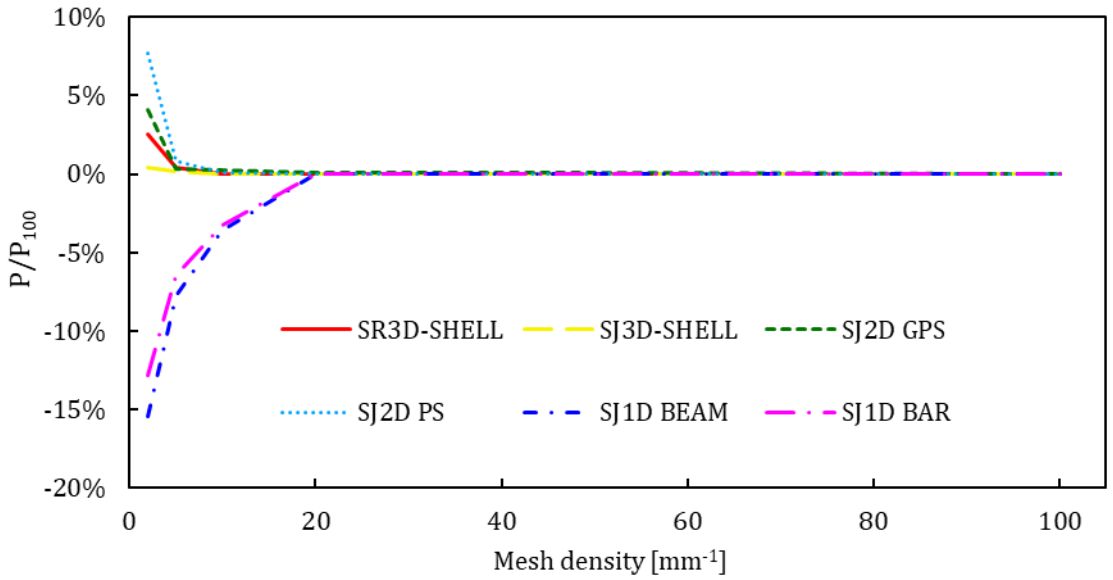

Figure 9: ME and FE mesh study. P is the strength of the joint for the current mesh density, and P_{100} the strength of the joint computed with a mesh density of 100 elements per mm.

3 Results and discussion

3.1 Stress analysis

Shear stress along the bondline computed by the two ME models and the four FE models were compared (Figure 10). To do so, the same force flow of 100 N/mm was applied to all models

and the shear stress was then extracted along the bondline. In the SJ3D-shell model, the shear stress was extracted both from the middle and the edge of the specimen to capture edge effects. In the SR3D-shell model, the shear stress was extracted from the section of the repair aligned with the direction of the load because this section is supposed to be the most loaded one. The shape of the shear stress distribution with series of stress peaks is typical of stepped joints because they behave like a series of single-lap-joints. All stress distributions were symmetrical about the middle of the joint expect in the SR3D-shell model. It was not surprising because this model was the only one not to be symmetrical due to the length outside the joint being higher on the parent plate side than on the repair patch side.

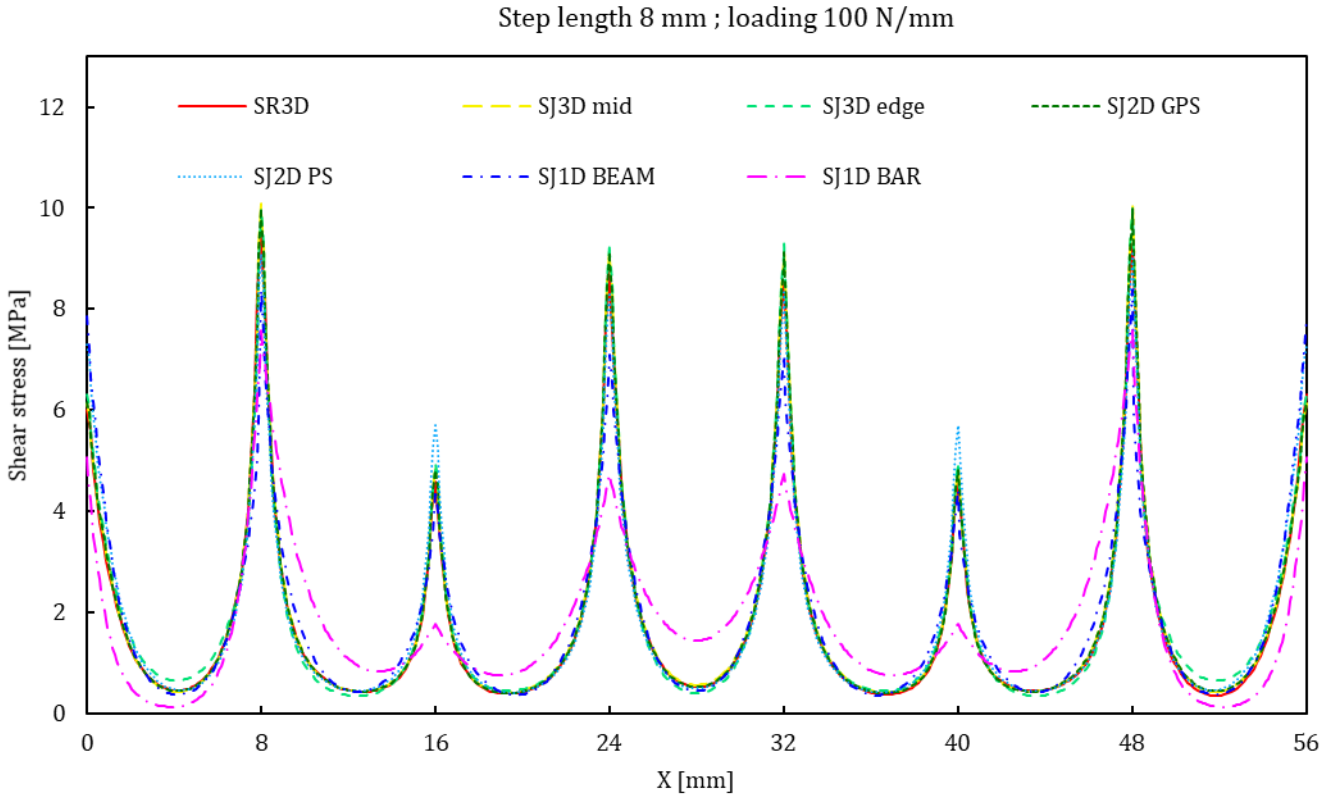

Figure 10: ME and FE shear stress distribution along the bondline

The ME SJ1D bar model had the lowest peak stresses and highest minimum stress. This flatter distribution was caused by stiffer adherends compared to the other models, which is reasonable because of the bar model does not allow bending and shear deformation of the adherends. The ME SJ1D beam model gave a better approximation of the bondline stresses. It was in good

agreement with FE at the two ends of the joints, but it underestimated the stress peaks in the middle, showing that it is still stiffer that FE models. Among FE models, a significant discrepancy was noted between SJ2D plane strain model and the other ones. It is because the plane strain state applied to composite woven laminates leads to a large increase of stiffness of the laminates due to the restriction of Poisson's effect. There was no clear deviation between the stresses extracted from the middle and the edge of the SJ3D-shell model, showing that there are negligible free-edge effects on the shear stress distribution. The SJ2D GPS was the closest to the SJ3D-shell and SR3D-shell models in terms of shear stress. This is in agreement with the result that was already established for scarf joints and scarf repairs in the literature [14]. The deviations between the presented models remained the same no matter the step length.

The analysis of the effect of step length on the shear stress distribution brought the classical result of the shear-lag approach [22], namely that maximum shear stress decreases when step length increases until a minimum is reached (Figure 11). No further decrease of peak shear stress was found beyond a step length of 8 mm. The deviations between the ME and FE models remained the same on the whole range of tested step length.

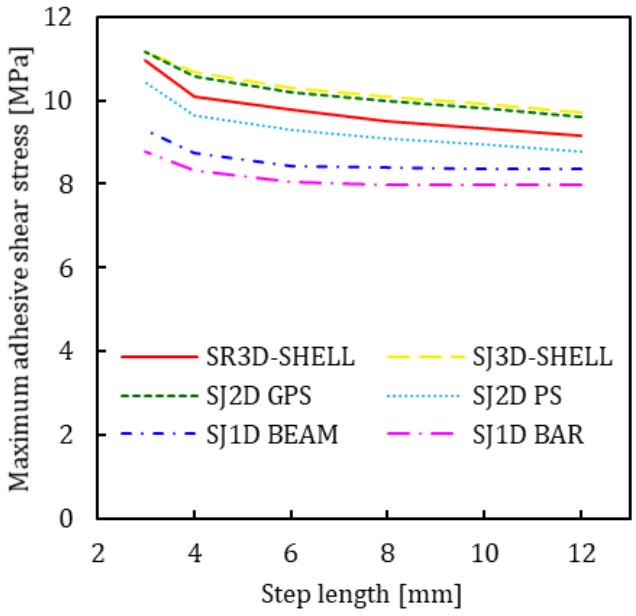

Figure 11: Effect of step length on maximum adhesive shear strain

3.2 Failure analysis

3.2.1 Damage scenario

Damage initiation location and propagation scenario was tracked in the FE models. Because of the shear stress peaks at the ends of the steps, several step end reached the maximum adhesive stress in early stages of the loading. Nonetheless, due to the fracture energy needed to propagate the crack in the adhesive layer, failure did not happen as soon as a region of the adhesive layer reached the maximum allowable stress. The sensitivity analysis revealed two different failure scenarios depending on the step length and the adhesive fracture energy (Figure 12). In both cases, reaching maximum load was followed by complete disbonding of the joint.

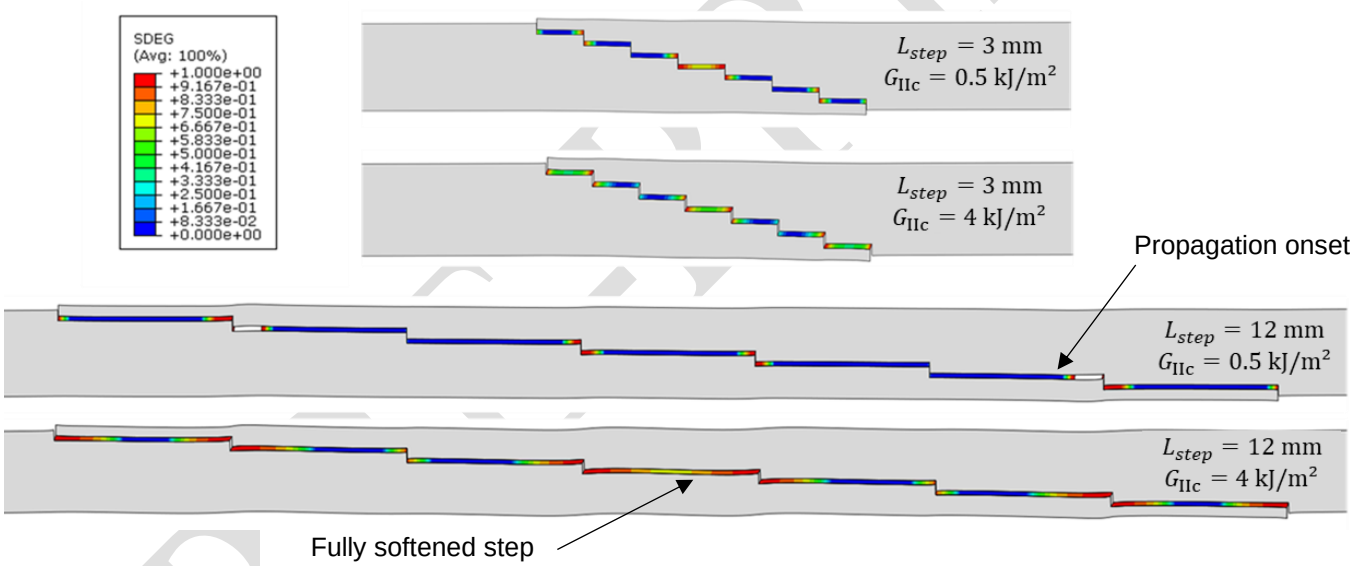

Figure 12: Damage propagation scenarios in the FE SJ3D-shell GPS model. Loading is 95% of failure load. SDEG is the scalar stiffness degradation coefficient of the interface.

The first scenario was failure of the adhesive layer by reaching maximum adhesive strain, or *fragile failure*. It happened when steps were long enough to allow the process zone reaching its maximum length in the most loaded area of the stepped joint, which is equivalent to reaching maximum adhesive strain. The crack that initiated at this point immediately propagated to the

whole step, leading to disbonding of the other steps and ultimately to total adhesive layer failure.

The second scenario was failure of the adhesive layer by softening of a whole step, or *ductile failure*. It happened when steps were short enough for two process zones to meet each other before reaching their maximum length, leading to complete loss of stiffness of one of the steps before reaching the adhesive maximum strain. At this point, the stepped joint reached an instability point causing subsequently failure of the entire adhesive layer. Reaching failure by softening of a whole step means that the load-carrying capacity of the stepped joint could have been theoretically increased until reaching failure by maximum adhesive strain. The location of disbonding initiation depended on the failure scenario. Due to the symmetrical nature of the stepped joints, damage would initiate and propagate simultaneously in a symmetrical pattern about the middle of the joint.

In case of fragile failure, the SJ2D GPS and SJ3D-shell model agreed on the damage initiation location. They both predicted it between the first and the second step. However, the SJ2D PS model predicted it at the beginning of the first step in the fragile configuration. It shows that the plane strain hypothesis does not only influence the stress distribution on the joint, but also the damage scenario, making that model not consistent with the others. The SR3D-shell model predicted the disbonding to begin between the first and the second step as well, but the 3D effects in that fragile scenario caused it not to propagate from the highest loaded section of the repair. Instead, the crack started to propagate in the area located at a 30° angle respectively to the direction of the load (Figure 13).

In case of ductile failure, the four FE models agreed on the damage scenario. Failure happened by full softening of the centre step of the repair. Edges effects in the SJ3D-shell model caused crack propagation along the coupon edges (Figure 14). Finally, the SJ2D GPS model was the

one which was the most consistent with the S3RD model in terms of damage propagation scenario no matter the step length or adhesive fracture toughness.

The same types damage propagation scenarios were observed in ME models, with *fragile* or *ductile* failure depending on adhesive properties and step length.

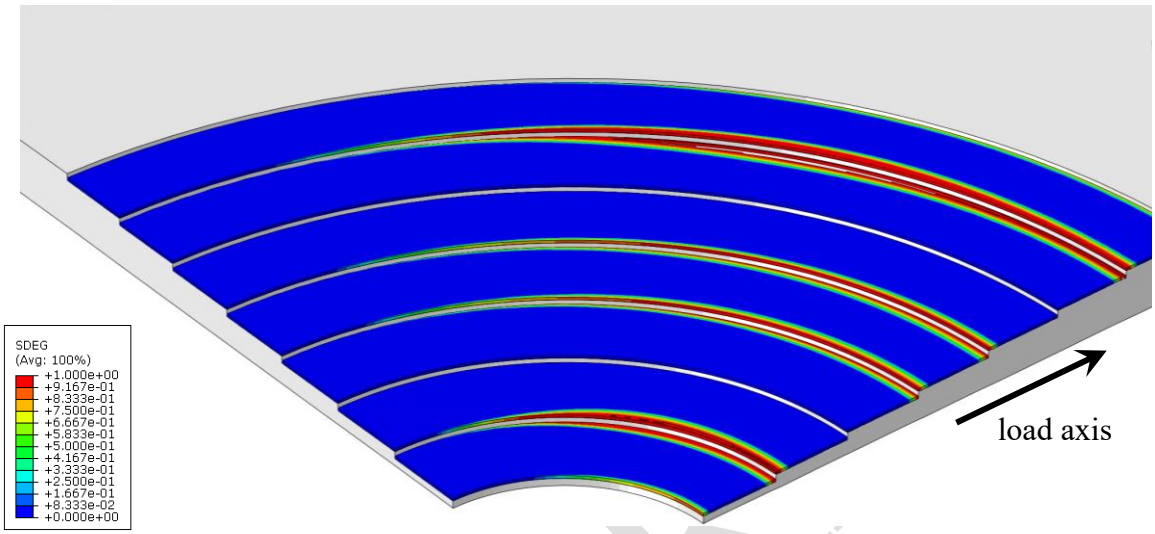

Figure 13 : Damage propagation scenario in the FE SR3D-shell model.

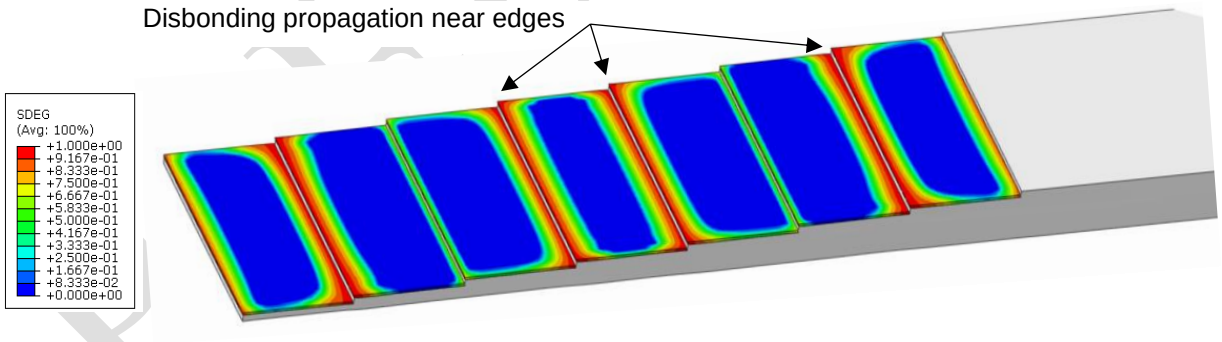

Figure 14 : Damage propagation scenario in the FE SJ3D-shell model.

3.2.2 Strength prediction

The results of each model were then compared in terms of predicted load-carrying capacity of the bonded joint (Figure 15).

Among FE models, the trend of the deviation between the four different models remained the same no matter the adhesive fracture toughness and step length:

- The SR3D-shell model was the one with the highest predicted strength. This is reasonable because the circular patch allows load bypass around the most loaded area of the repair.
- The SJ3D-shell model was the FE model with the lowest predicted strength. This is related to edges effects provoking crack propagation on the edges of the stepped joint (section 3.2.1), leading to anticipated failure of the joint in this model. It is interesting to remind that those edge effects did not appear in the stress analysis.
- The SJ2D PS predicted strength was greater than the SJ3D-shell strength and lower than SJ2D GPS strength. For most of the considered step lengths, there was a larger deviation between the SJ2D PS and SJ2D GPS models when the adhesive is fragile. This is explained by the inconsistency between the failure scenarios of the SJ2D PS model and the SJ2D GPS model, as explained in section 3.2.1, paragraph 4.
- The SJ2D GPS model was the closest to the SR3D-shell in any case, capturing accurately the trend of its strength / step length curve and strength / G_{IIC} curve. (Figure 15). The only case where the deviation between those two models exceeded 5% was with a step length of 12 mm and G_{IIC} = 0.25 kJ/m².

ME models globally underestimated the joint strength compared to FE models even though they had lower stress peaks. This was quite surprising but could be explained by the fact that they neglected shear deformation of the adherends, which tend to increase process zones length and decrease predicted strength. The SJ1D beam model was more conservative than SJ1D bar model. This is consistent with the fact that the SJ1D beam model includes peels effect and predicts higher stress peaks than the SJ1D model (section 3.1.). The deviation trend between FE and ME models remained fairly the same for all the step lengths and adhesive fracture toughness tested, except in the case of steps shorter than 4 mm and brittle adhesive material with $G_{\mathrm{IIC}} \leq 0.5\ \mathrm{kJ/m^2}$. In that case, the deviation was reversed and the SJ1D bar and beam

models became more conservative than FE models. Indeed, brittle adhesive material properties decrease process zone length, and short steps increase stress peaks. It makes that configuration close to a purely fragile situation, where failure is driven by maximum stress only. Given that ME models tend to underestimate shear stress compared to FE models, it explains why ME predicted lower strength than FE with those parameters.

The sensitivity analysis showed as expected that the strength of the joint increases when the step length or adhesive fracture toughness increases (Figure 15). Joint strength / G_{IIC} curves (Figure 15 a-b-c) show that the deviation between all models remains consistent when G_{II} changes, expect in the case of 3 mm steps and low fracture energy already mentioned. It demonstrates that simplified models of a stepped repair are robust against a change of adhesive material properties.

The strength / step length curves with G_{IIC} = 1 kJ/m² (Figure 15 e) show that joint strength reached a plateau for long steps, beyond which an increase of step length brings no further increase of joint strength. This strength plateau appears when the steps are longer than the process zones. It makes the behaviour of a stepped joint comparable to of a single or double lap joint. Indeed, Hart-Smith [23] showed that when the joint is longer than a critical length depending on G_{IIC}, there is no further increase in joint strength. This is related to the change of failure mode between what we call *fragile failure* and *ductile failure* of the joint in this paper. Moreover, the dispersion in predicted strength between the tested models increases largely when transition from one failure scenario to the other. The same plateau effect was expected for fragile adhesives, but the strength/step length curves with $G_{IIC} = 0.25\ \mathrm{kJ/m^2}$ (Figure 15 d) show that ME SJ1D models reached a strength plateau for steps longer than 6 mm whereas the joint strength predicted by SR3D-shell and SJ2D GPS kept on increasing until a step length of 12 mm. The strength/step length curves with G_{IIC} = 4 kJ/m² (Figure 15 f) shows that no plateau

is reached, meaning that typical step lengths are not sufficient to achieve the maximum potential joint strength that could be reached with a ductile adhesive material.

To give a better picture of the deviations between all the tested models, the mean absolute deviation in terms of strength was computed between each of them and the SR3D-shell, which was chosen to be the reference (Table 4). Again, the SJ2D GPS clearly stands out as the closest to the SR3D-shell model for repair strength prediction.

Table 4 : Mean absolute deviation between strength predicted by stepped joint models and FE 3D stepped repair model

Model	Mean abs. deviation vs SR3D-shell	Maximum abs. deviation vs SR3D-shell
SJ1D bar	8.6%	20.1%
SJ1D beam	11.1%	23.2%
SJ2D PS	5.5%	11.1%
SJ2D GPS	2.7%	7.8%
SJ3D-shell	8.7%	19.3%

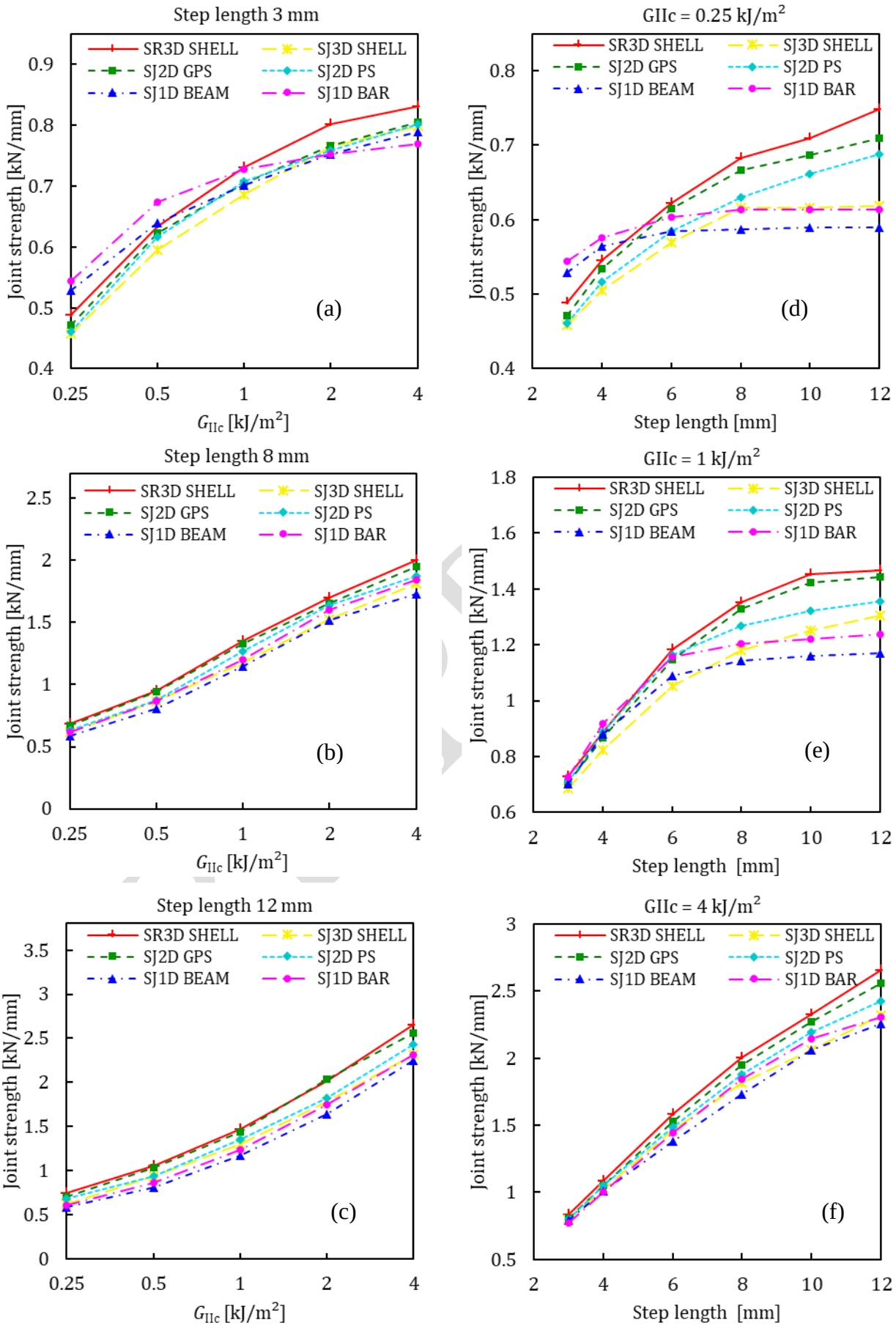

Figure 15: Comparison between strength predicted by ME and FE models. In graphs (a), (b) and (c) G_{IIc} is in logarithmic scale in abscissa and step length is fixed. In graphs (d), (e) and (f) step length is in linear scale in abscissa and G_{IIc} is fixed.

3.3 Discussion on results sensitivity to cohesive law parameters

3.3.1 Mixed-mode propagation law

In the main part of this study, a linear energetic criterion was used for the mixed-mode propagation behaviour of the cohesive elements (Eq. 21). This criterion is not the only one to be used to model adhesive behaviour. To do so we can cite other criteria, such as quadratic energetic criterion:

$$\left(\frac{G_{\mathrm{I}}}{G_{\mathrm{IC}}}\right)^2 + \left(\frac{G_{\mathrm{II}}}{G_{\mathrm{IIC}}}\right)^2 = 1 \tag{22}$$

or Benzeggagh-Kenane (BK) criterion:

$$G_{\mathrm{C}} = G_{\mathrm{IC}} + (G_{\mathrm{IIC}} - G_{\mathrm{IC}})\left(\frac{G_{\mathrm{II}}}{G_{\mathrm{I}} + G_{\mathrm{II}}}\right)^{\eta} \tag{23}$$

To assess the robustness of the parametric study that was performed, the influence of the choice this criterion was tested using the SJ2D-GPS model. Stepped joint strength calculation were performed in the exact same way as before with the quadratic energy criterion and the BK criterion, for a step length of 8 mm, and a range of G_{IIC} between 0.25 and 4 kJ/m². The results are presented in Figure 16. It appears that the choice of the mixed-mode propagation law has only very little influence on the results. This is understanble as main point of a stepped joint geometry compared to a single-lap joint for example is to minimize the peeling effects. As a consequence, G_{C} ends up being very close to G_{IIC} no matter the criterion used. It can be noted that there is slightly more influence of the criterion when the adhesive is more brittle, but it remains barely noticeable.

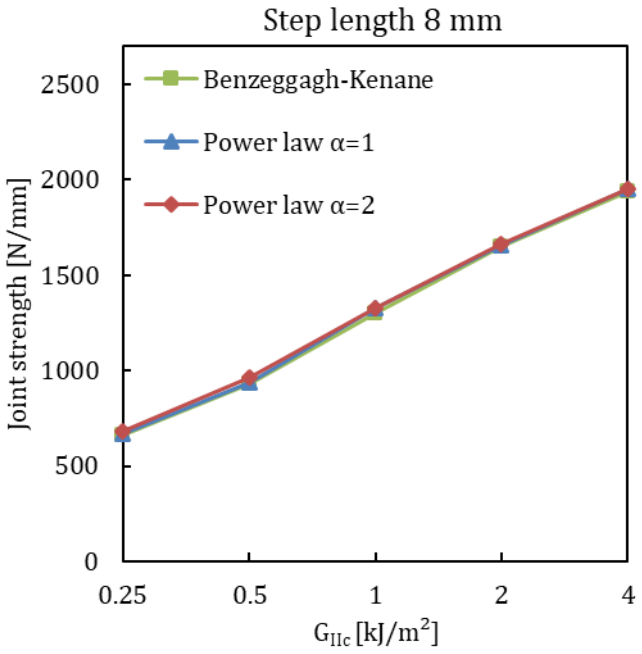

Figure 16: Comparison of the predicted joint strength for Benzeggagh-Kenane and power law propagation criteria

3.3.2 CZM law shape

In this study, CZM laws used for the adhesive had a triangular shape, with constant damage initiation stresses σ_{I}^{0} and σ_{II}^{0}, interfaces stiffness k_{I} and k_{II}, and constant ratio $G_{\mathrm{IIC}}/G_{\mathrm{IC}} = 2$. The only variable parameter of the cohesive law was G_{IIC} and it was used to drive the ductility of the adhesive. However, the use of trapezoidal law shapes is sometimes preferred to triangular law shapes to model the behaviour of ductile adhesives materials. Therefore, a discussion on the influence of the law shape on the strength prediction of a stepped joint, in the case of ductile adhesive, is provided hereafter. To do so, two trapezoidal law shapes TPZ-1 and TPZ-2 were tested to compare to results obtained in term of predicted strength of the stepping joint against the reference value previously obtained with the triangular law and $G_{\mathrm{IIC}} = 4\ \mathrm{kJ/m^2}$ and a step length of 8 mm.

The definition of TPZ-1 and TPZ-2 laws is presented for pure mode II (Figure 17). The same is done in pure mode I with $G_{\mathrm{IIC}}/G_{\mathrm{IC}} = 2$. TPZ-1 was defined to match the interface stiffness

and damage initiation stress of the triangular law. The softening slope was chosen to be equal to the one in the case of the triangular law with $G_{\mathrm{IIC}} = 1\ \mathrm{kJ/m^2}$ and end displacement of adjusted to keep $G_{\mathrm{IIC}} = 4\ \mathrm{kJ/m^2}$. TPZ-2 was defined using the same interface stiffness and softening slope, but this time the end displacement was kept equal to the one of the reference triangular law, and the maximum stress was adjusted to match $G_{\mathrm{IIC}} = 4\ \mathrm{kJ/m^2}$. All the properties are summed up in table 4.

Table 4: Trapezoidal CZM parameters for laws TPZ-1, TPZ-2 and the reference triangle law

Property	Symbol (units)	TPZ-1		TPZ-2		Triangle	
		Mode I	Mode II	Mode I	Mode II	Mode I	Mode II
Interface stiffness	k_i (MPa/mm)	20000	6667	20000	6667	20000	6667
Fracture toughness	G_{iC} (kJ/m^2)	2	4	2	4	2	4
Initiation stress	σ_{I}^0 (MPa)	48	40	23.5	21.4	48	40
Softening onset	δ_{i}^1 (mm)	0.018	0.081	0.074	0.176	-	-
End displacement	δ_{I}^f (mm)	0.072	0.125	0.1	0.2	0.1	0.2

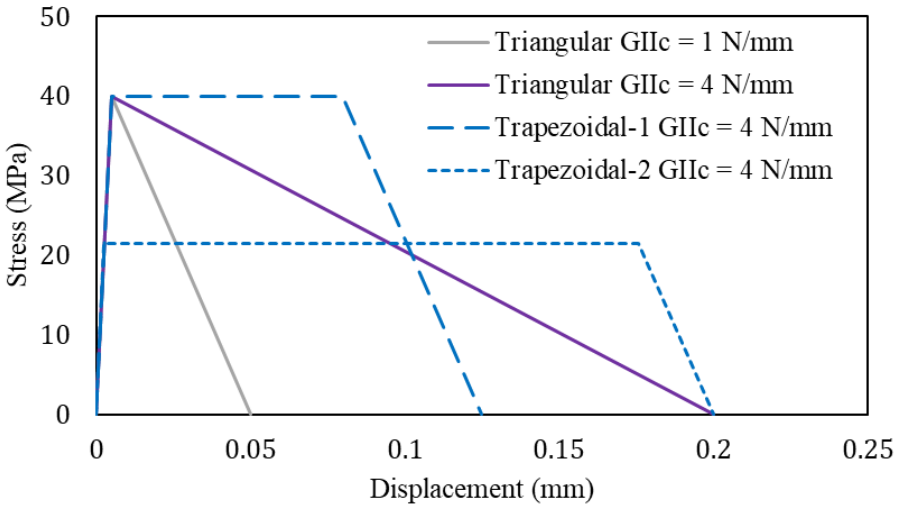

Figure 17 : Pure mode II representation of the triangular and trapezoidal law shapes used

For mixed-mode behaviour (Figure 18), damage initiation stress is defined using quadratic stress criterion (Eq. 20), damage propagation energy is defined using linear energetic criterion (Eq. 21), and the softening onset is defined using the following criterion:

$$\left(\frac{\delta_{\mathrm{I,m}}^{1}}{\delta_{\mathrm{I}}^{1}}\right)^{2}+\left(\frac{\delta_{\mathrm{II,m}}^{1}}{\delta_{\mathrm{II}}^{1}}\right)^{2}=1$$

Where δ_{I}^{1} $(i=\mathrm{I},\mathrm{II})$ is the relative displacement at initiation of stress softening in each pure mode, and $\delta_{\mathrm{I,m}}^{1}$ $(i=\mathrm{I},\mathrm{II})$ are the corresponding mixed-mode displacement.

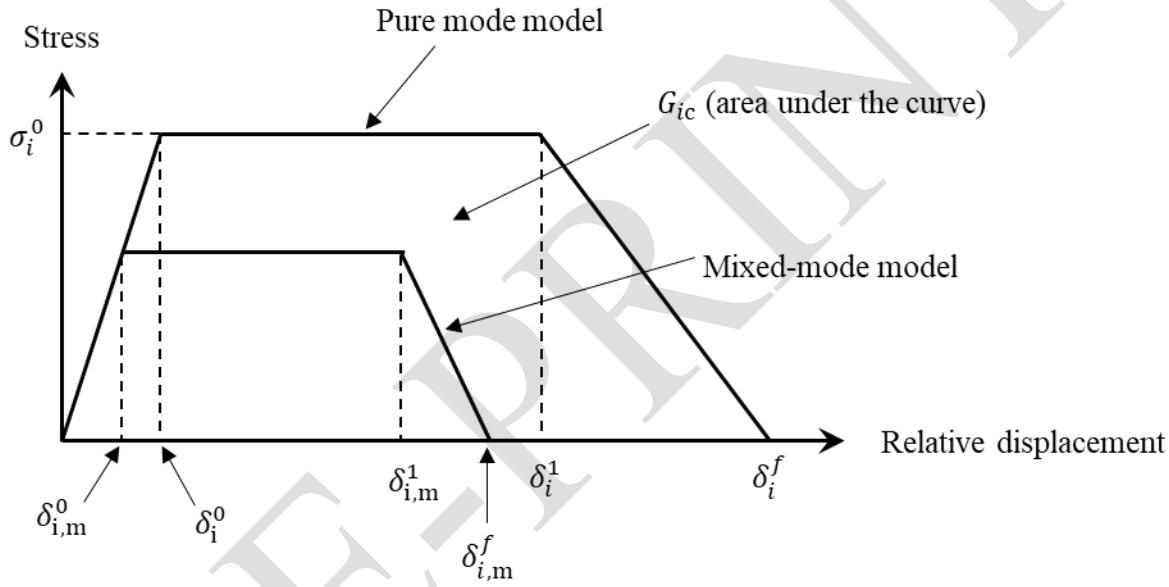

Figure 18: Trapezoidal cohesive law, in pure and mixed mode

The results are the following: TPZ-1 law brings an increase of 6% in term of predicted strength of the stepped joint, while TPZ-2 brought a decrease of 5% in terms of predicted strength of the stepped joint for a step length of 8 mm (Figure 19). These results are understandable because the initial triangular law is framed by the two trapezoidal law we proposed. As seen in section 3.2.1, the final failure happens when the stepped joint reaches an instable state, which is driven by the length of the process zones when the adhesive is ductile. The shape of the CZM laws influences the process zones lengths, this explains why the final strength of the joint is affected by the law shape. Therefore, it can be concluded that the use of a trapezoidal law affects slightly the results compared to a triangular law shape, but the deviation depends on the trapezoidal law

parameters. Given that the triangular laws results lies between the results given by the two trapezoidal laws tested, with constant initiation stress and constant end-displacement, it is reasonable to say that a triangular law was suitable to model the behaviour of a ductile adhesive material is the study.

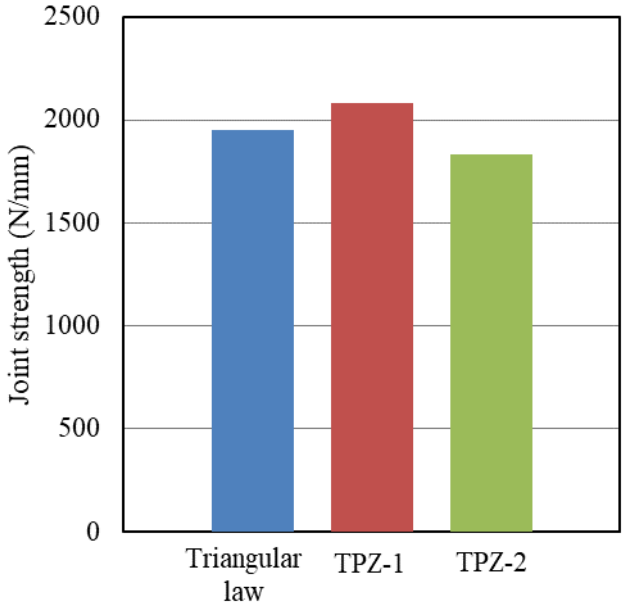

Figure 19: Comparison between the predicted strength of a stepped joint with different CZM laws. Step length is 8mm and G_{IIc} = 4 N/mm.

4 Conclusions

The results of a 3D FE stepped repair model were compared to five simplified stepped joint models in terms bondline stress and failure strength. Different degrees of simplification, going from 3D FE modelling to 1D macro-element modelling were proposed. Non-linear simulations were done with all bonded zones modelled by cohesive behaviour.

A stress analysis highlighted that there is very little deviation between the bondline stress in FE models. It confirmed that the stress state in a simplified stepped joint model is close to the one in the most loaded area of a stepped repair. However, ME models significantly underestimated bondline stress compared to FE models. Failure scenarios and predicted strength of each model

were then compared on a large range of step lengths and adhesive fracture toughness. All simplified models were conservative respectively to the 3D stepped repair model. 2D stepped joint FE modelling under plane strain hypothesis modified the composite plies stiffness, which led this model to predict failure scenarios in disagreement with the other models tested. The use of generalized plane strain state seems to be the best option to model a 2D stepped joint representative for the behaviour of a 3D stepped repair: it is consistent with the full 3D model in terms of failure scenario, has less than 3% average absolute deviation compared to the latter, and saves significant computing time. 3D stepped joint modelling induced edges effects that lead to anticipated failure in this model. Therefore, it makes sense using 3D modelling to assess the strength of a stepped joint coupon, but it does not in the case if it is used to study the strength of a stepped repair.

Macro-element modelling of a stepped joint is unexpectedly conservative most of the time compared to FE models, expect for short step length and fragile adhesive. The beam model is even more conservative than the bar model. There is up to 20% deviation between ME models and FE in the case of fragile adhesive and long steps. This shows that ME could be suitable for strength prediction of stepped repair, but one can say that their area of validity is restricted to ductile enough adhesives.

This work could be pursued by running more simulations with various stacking sequences or with different types of composite materials, and by performing experimental testing of stepped joints, stepped-repaired coupons and stepped repaired panels.

5 Acknowledgement

The authors would like to thank Direction Générale de l'Armement, part of French ministry of Defence, and ISAE-SUPAERO for their financial support.

6 References

[1] Heslehurst RB. Engineered Repairs of Composite Structures. CRC Press; 2019. https://doi.org/10.1201/9780429198656.

[2] Ahn S-H, Springer G. Repair of Composite Laminates-II: Models. J Compos Mater 1998;32(11):1076–1114. https://doi.org/10.1177/002199839803201103.

[3] Wang CH, Gunnion AJ. On the design methodology of scarf repairs to composite laminates. Compos Sci Technol 2008;68(1):34–46. https://doi.org/10.1016/J.COMPSCITECH.2007.05.045.

[4] Xiaoquan C, Baig Y, Renwei H, Yujian G, Jikui Z. Study of tensile failure mechanisms in scarf repaired CFRP laminates. Int J Adhes Adhes 2013;41:177–185. https://doi.org/10.1016/j.ijadhadh.2012.10.015.

[5] Psarras S, Loutas T, Papanaoum M, Triantopoulos OK, Kostopoulos V. Investigating the effect of stepped scarf repair ratio in repair CFRP laminates under compressive loading. J Compos Sci 2020;4:153. https://doi.org/10.3390/jcs4040153.

[6] Hayes-Griss JM, Orifici AC, Khatibi AA. An improved progressive failure modelling and damage tolerant design methodology for composite scarf joints with bondline flaws. Composites Part A 2020;131:105776. https://doi.org/10.1016/j.compositesa.2020.105776.

[7] Pinto AMG, Campilho RDSG, de Moura MFSF, Mendes IR. Numerical evaluation of three-dimensional scarf repairs in carbon-epoxy structures. Int J Adhes Adhes 2010;30(5):329–337. https://doi.org/doi:10.1016/j.ijadhadh.2009.11.001.

[8] Pierce RS, Falzon BG. Modelling the size and strength benefits of optimised step/scarf joints and repairs in composite structures. Composites Part B 2019;173:107020. https://doi.org/10.1016/j.compositesb.2019.107020.

[9] Orsatelli JB, Paroissien E, Lachaud F, Schwartz S. Bonded flush repairs for aerospace composite structures: a review on modelling strategies and application to repairs optimization, reliability and durability. Comp Struct 2023;304:116338. https://doi.org/10.1016/j.compstruct.2022.116338

[10] Wang S, Xie Z, Li X. On adhesively bonded stepped-scarf joint: an analytical model and its validation. Mech Adv Mater Struct 2019;28:938–951. https://doi.org/10.1080/15376494.2019.1614699.

[11] Soutis C, Hu FZ. Failure Analysis of Scarf-Patch-Repaired Carbon Fiber/Epoxy Laminates Under Compression. AIAA J 2000;38(4):737–740. https://doi.org/https://doi.org/10.2514/2.1027.

[12] Gunnion AJ, Herszberg I. Parametric study of scarf joints in composite structures. Compos Struct 2006;75(1):364–376. https://doi.org/10.1016/j.compstruct.2006.04.053.

[13] Liu B, Xu F, Feng W, Yan R, Xie W. Experiment and design methods of composite scarf repair for primary-load bearing structures. Composites Part A 2016;88:27–38. https://doi.org/10.1016/j.compositesa.2016.05.011

[14] Tashi S, Abedian A. A comprehensive 2 Dimensional and 3 Dimensional FE study of scarf repair for a variety of common composite laminates under in-plane uniaxial and equibiaxial loadings. Int J Adhes Adhes 2022;114:103092. https://doi.org/10.1016/j.ijadhadh.2022.103092.

[15] Damghani M, Bakunowicz J, Murphy A. Understanding the influence of laminate stacking sequence on strain/stress concentrations in thin laminates at repair holes with large scarf angles. J Compos Mater 2019;53(28–30):4273–84. https://doi.org/10.1177/0021998319855772.

[16] Deleris M, Cénac F. Method for repairing a wall consisting of a plurality of layers. Patent CA 2769668A1 A1 2011/02/17.

[17] Collombet F, Davila Y, Avila S, Morales A, Crouzeix L, Grunevald YH, Hernandez H, Rocher N, Cénac F. Proof of a composite repair concept for aeronautical structures: a simplified method. Mechanics & Industry 2019:20(8):812. https://doig.org/10.1051/meca/2020056

[18] HEXCEL. HexPlyM18/1 180 Degree Celcius Curing Epoxy Matrix Product Data ; HEXCEL : Stamford CT, USAE, 2011.

[19] Paroissien E, Lachaud F, Schwartz S. Modelling load transfer in single-lap adhesively bonded and hybrid (bolted / bonded) joints. Prog Aerosp 2022;130:100811 https://doi.org/10.1016/j.paerosci.2022.100811

[20] Lélias G, Paroissien E, Lachaud F, Morlier J, Schwartz S, Gavoille C. An extended semi-analytical formulation for fast and reliable mode I/II stress analysis of adhesively bonded joints. Int J Solids Struct 2015;62:18–38. https://doi.org/10.1016/j.ijsolstr.2018.09.005

[21] Turon A, Davila CG, Camanho PP, Costa J. An engineering solution for mesh size effects in the simulation of delamination using cohesive zone models. Eng Frach Mech 2007 ;74 :1665-1682 https://doi.org/10.1016/j.engfracmech.2006.08.025

[22] Volkersen O. Die Nietkraftverteilung in zugbeanspruchten Nietverbindungen mit konstanten Laschenquerschnitten. Lufsfarhtforschung 1938:15:41-47.

[23] Hart-Smith LJ. Adhesive-bonded double lap joints. Douglas Aircraft Co, NASA Langley report CR-112235, 1974.

7 Appendix A: Coupling matrix of 1D bar ME

In order to determine the stiffness matrix K_e that links the displacement vector U_e to the nodal force vector F_e such that $F_e = K_e U_e$, two coupling matrices L_e and D_e^{-1} are obtained using the constitutive relationships in equations (1) and (2) :

$$C = D_e^{-1} U_e \Leftrightarrow \begin{pmatrix} c_1 \\ c_2 \\ c_3 \\ c_4 \end{pmatrix} = \begin{pmatrix} 1-\chi & 1+\chi & 0 & 0 \\ -\dfrac{1-\chi}{\Delta} & -\dfrac{1+\chi}{\Delta} & \dfrac{1-\chi}{\Delta} & \dfrac{1+\chi}{\Delta} \\ -\dfrac{e^{\eta\Delta}}{2\sinh\eta\Delta} & \dfrac{e^{\eta\Delta}}{2\sinh\eta\Delta} & \dfrac{1}{2\sinh\eta\Delta} & -\dfrac{1}{2\sinh\eta\Delta} \\ \dfrac{e^{-\eta\Delta}}{2\sinh\eta\Delta} & -\dfrac{e^{\eta-\Delta}}{2\sinh\eta\Delta} & -\dfrac{1}{2\sinh\eta\Delta} & \dfrac{1}{2\sinh\eta\Delta} \end{pmatrix} \begin{pmatrix} u_1(0) \\ u_2(0) \\ u_1(\Delta) \\ u_2(\Delta) \end{pmatrix}$$

$$F_e = L_e C \Leftrightarrow \begin{pmatrix} -N_1(0) \\ -N_2(0) \\ N_1(\Delta) \\ N_2(\Delta) \end{pmatrix} = \frac{1}{2} \begin{pmatrix} 0 & -A_1 & -\eta(1+\chi)A_1 & \eta(1+\chi)A_1 \\ 0 & -A_2 & \eta(1-\chi)A_2 & -\eta(1-\chi)A_2 \\ 0 & A_1 & \eta(1+\chi)e^{-\eta\Delta}A_1 & -\eta(1+\chi)e^{\eta\Delta}A_1 \\ 0 & A_2 & -\eta(1-\chi)e^{-\eta\Delta}A_2 & \eta(1-\chi)e^{\eta\Delta}A_2 \end{pmatrix} C$$

where Δ is the length of the bonded zone.